A numerical and experimental study on the nonlinear evolution of long-crested irregular waves

Arnaud Goullet[1] and Wooyoung Choi[1,2]
[1]*Department of Mathematical Sciences, Center for Applied Mathematics and Statistics, New Jersey Institute of Technology, Newark, New Jersey 07102-1982, USA*
[2]*Division of Ocean Systems Engineering, Korea Advanced Institute of Science and Technology, Daejeon 305-701, Korea*

(Received 15 June 2010; accepted 10 December 2010; published online 6 January 2011)

The spatial evolution of nonlinear long-crested irregular waves characterized by the JONSWAP spectrum is studied numerically using a nonlinear wave model based on a pseudospectral (PS) method and the modified nonlinear Schrödinger (MNLS) equation. In addition, new laboratory experiments with two different spectral bandwidths are carried out and a number of wave probe measurements are made to validate these two wave models. Strongly nonlinear wave groups are observed experimentally and their propagation and interaction are studied in detail. For the comparison with experimental measurements, the two models need to be initialized with care and the initialization procedures are described. The MNLS equation is found to approximate reasonably well for the wave fields with a relatively smaller Benjamin–Feir index, but the phase error increases as the propagation distance increases. The PS model with different orders of nonlinear approximation is solved numerically, and it is shown that the fifth-order model agrees well with our measurements prior to wave breaking for both spectral bandwidths. © *2011 American Institute of Physics*. [doi:10.1063/1.3533961]

I. INTRODUCTION

It is crucial to accurately predict ocean waves for surface ships and offshore structures operating in severe sea states where extreme events such as rogue waves could occur. These rare, but highly destructive phenomena have been observed more frequently than ever imagined. In recent years, considerable progress toward more accurate predictions of such waves has been made using various mathematical models and numerical methods. Among them, for the phase-resolving prediction of broadband nonlinear surface waves, a pseudospectral (PS) method based on the asymptotic formulation of West *et al.*[1] has been found to be an accurate and computationally efficient numerical tool when combined with fast Fourier transform (Bateman *et al.*[2] and Tanaka[3,4]). The formulation of West *et al.*[1] is closely related to that of Craig and Sulem,[5] who expanded formally the Dirichlet–Neumann operator for water of finite depth. Similar pseudospectral approaches have been also proposed by Dommermuth and Yue[6] and Clamond and Grue.[7] These pseudospectral formulations have been further generalized to investigate the interaction of nonlinear waves with bottom topography (Smith,[8] Craig *et al.*,[9] and Guyenne and Nicholls[10]) and with a submerged body (Liu *et al.*[11] and Kent and Choi[12]). Numerical solutions of these pseudospectral models have been widely validated with numerical solutions obtained via classical boundary element methods and laboratory experiments in, e.g., Bateman *et al.*,[2] Choi *et al.*,[13] Fructus *et al.*,[14] Tian *et al.*,[15] and Xu and Guyenne.[16] A drawback of this approach (or any Eulerian approaches) is that, once the wave slope becomes large so that wave breaking occurs, no reliable computations can be made. Recently, an attempt to take into account energy dissipation due to wave breaking was made by Tian *et al.*[17] for focusing wave groups using an eddy viscosity model. Surprisingly, when the eddy viscosity is estimated from measured energy dissipation due to wave breaking, their numerical solution for the surface elevation at wave probes located downstream of the active breaking region shows excellent agreement with laboratory measurements.

A spectral formulation of Zakharov[18] accurate to the third order in wave steepness has been also adopted to study the evolution of broadband nonlinear surface waves. This formulation has been modified to include the next-order terms (Krasitskii[19,20] and Stiassnie and Shemer[21]). In Shemer *et al.*,[22] it was shown that their numerical solutions of the modified Zakharov equation compare well with experimental measurements for the propagation of slowly modulated wave packets. Although it has been used to study the evolution of broadband nonlinear surface waves (Yokoyama[23]), these spectral formulations require one to evaluate multiple convolution integrals, which is computationally expensive, and, therefore, has been used with lower-order nonlinear approximations. Since the wave fields in our laboratory experiments are often so nonlinear that higher-order nonlinear (e.g., fifth- or seventh-order) effects need to be included, the spectral formulation of Zakharov is not considered in this paper.

A simpler model was also suggested by Zakharov[18] to describe the evolution of the envelope of slowly modulated surface waves. Under the weakly nonlinear and narrow-bandness assumptions, it is well-known that the slowly varying envelope is governed by the nonlinear Schrödinger (NLS) equation that is valid up to the third-order in wave steepness, $\epsilon \ll 1$ with assuming the spectral bandwidth to be $O(\epsilon)$. Compared with the aforementioned pseudospectral or

spectral approaches, the NLS-type equation has been widely adopted due to its simplicity, for numerical studies, but has been known to fail to describe accurately the observed evolution of real nonlinear wave packets. For example, the front-tail asymmetry of nonlinear wave packets observed in laboratory experiments is not captured by the NLS equation, as discussed in Shemer *et al.*[24] The NLS equation was extended by Dysthe[25] with including the fourth-order corrections and the resulting fourth-order equation is often referred to as the modified nonlinear Schrödinger (MNLS) equation. This model has been further generalized by relaxing the constraint on the bandwidth to $O(\epsilon^{1/2})$ by Trulsen and Dysthe.[26] Compared with that of the NLS equation, the numerical solutions of the MNLS equation were found to agree better with laboratory experiments over a longer distance, as demonstrated by Lo and Mei[27] and Shemer *et al.*[28] for slowly modulated wave packets and Trulsen and Stansberg[29] for bichromatic waves. Clamond *et al.*[30] compared the numerical solutions of the NLS and MNLS equations with those of the PS models of both West *et al.*[1] and Clamond and Grue[7] for the long-term propagation of envelope solitary waves and found that these weakly nonlinear models are of limited success in real applications.

Up until now, validation or invalidation of various nonlinear wave models with laboratory experiments has been made mostly for wave fields with a small number of frequency components. Even with a large number of frequency components, instead of generating them at the wavemaker in a random fashion, a frequency focusing technique is often used for a large peak to form at a prescribed location (Johannessen and Swan,[31–33] Shemer *et al.*,[34] and Tian *et al.*[15]). A relatively less number of attempts have been made to validate nonlinear wave models with laboratory experiments for the evolution of *true* broadband irregular waves, in particular, when the wave steepness is finite.

An earlier attempt to validate numerical solutions with laboratory experiments for broadband wave fields was made by Spell *et al.*[35] for a wave field characterized by the JONSWAP spectrum whose wave steepness is $\epsilon_p=0.12$, where the wave steepness is defined as $\epsilon_p=k_pH_s/2$ with k_p and H_s being the peak wave number and the significant wave height, respectively. They used a second-order nonlinear wave theory of Zhang *et al.*[36] and found that the comparison was reasonable up to a relatively short distance of $k_px/(2\pi)=1.88$, where x is the downstream wave probe location. We should remark that a typical wave steepness for our experiments is $\epsilon_p=0.2$ and the comparison is made up to a relatively longer distance of $k_px/(2\pi)=14.6$. Similarly, Bonnefoy *et al.*[37] made a preliminary comparison of a second-order spectral model[38] for a surface wave field created by a Bretschneider spectrum, but their characteristic steepness was smaller than what we consider in this paper. In Grue *et al.*,[39] the velocity profile measurements using particle image velocimetry under broadband wave fields of $\epsilon_p=0.1-0.15$ were found reasonable agreement with the numerical solutions of the pseudospectral model of Clamond and Grue,[7] but no comparison of the surface elevation has been presented. The NLS and MNLS equations have been also tested, but previous studies using these models have focused on the time evolution of wavenumber spectrum (Dysthe *et al.*[40] and Socquet-Juglard *et al.*[41]) and statistical properties of wave fields, such as the correlation between kurtosis and the occurrence of extreme events or rogue waves.[42,43]

In this paper, we adopt a phase-resolving PS model based on the formulation of West *et al.*[1] and study numerically the evolution of moderately nonlinear wave fields of $\epsilon_p=0.2$. We compare our numerical solutions with new laboratory experiments and address its capability to predict broadband wave fields in comparison with the MNLS model.

The paper is organized as follows. In Sec. II, the two mathematical models (the PS model and the MNLS equation) are described along with the numerical methods adopted in this paper. After we outline our experimental setup and describe our observations in Sec. III, we present our numerical solutions compared with experimental measurements in Sec. IV.

II. MATHEMATICAL MODELS AND NUMERICAL METHODS

A. A pseudospectral model

For inviscid, incompressible, and irrotational flows in water of uniform depth h, by assuming that the waves have small steepness $\epsilon=a/\lambda$ with a and λ being a characteristic amplitude and wavelength, respectively, the free surface motions are governed by the following set of nonlinear evolution equations:[1]

$$\frac{\partial\zeta}{\partial t}=\sum_{n=1}^{\infty}Q_n[\zeta,\Phi],\quad \frac{\partial\Phi}{\partial t}=\sum_{n=1}^{\infty}R_n[\zeta,\Phi], \tag{1}$$

where $\zeta(\boldsymbol{x},t)$ is the surface elevation and $\Phi(\boldsymbol{x},t)\equiv\phi(\boldsymbol{x},z=\zeta,t)$ is the velocity potential evaluated at the free surface. In Eq. (1), Q_n and R_n are given by the following explicit recursion formulas:

$$Q_1=W_1,\quad Q_2=W_2-\nabla\Phi\cdot\nabla\zeta,$$

$$Q_n=W_n+|\nabla\zeta|^2W_{n-2}\quad\text{for } n\geq 3, \tag{2}$$

$$R_1=-g\zeta,\quad R_2=-\frac{1}{2}|\nabla\Phi|^2+\frac{1}{2}W_1^2,\quad R_3=W_1W_2,$$

$$R_n=\frac{1}{2}\sum_{j=0}^{n-2}W_{n-j-1}W_{j+1}+\frac{1}{2}|\nabla\zeta|^2\sum_{j=0}^{n-4}W_{n-j-3}W_{j+1}$$

$$\text{for } n\geq 4, \tag{3}$$

where $\boldsymbol{\nabla}=(\partial x,\partial y)$ represents the horizontal gradient. This system can be derived from the nonlinear free surface boundary conditions written in terms of ζ, Φ, and the vertical velocity evaluated at the free surface W,

$$\frac{\partial \zeta}{\partial t} + \nabla\Phi \cdot \nabla\zeta = (1 + |\nabla\zeta|^2)W,$$
$$\frac{\partial \Phi}{\partial t} + \frac{1}{2}|\nabla\Phi|^2 + g\zeta = \frac{1}{2}(1 + |\nabla\zeta|^2)W^2, \tag{4}$$

by substituting into Eq. (4) the expansion of W in Taylor series about $z=0$,

$$W = \sum_{n}^{\infty} W_n[\zeta,\Phi], \tag{5}$$

where $W_n = O(\epsilon^n)$ are given in Appendix A. Notice that $Q_n = O(R_n) = O(\epsilon^n)$. The leading-order terms (Q_1 and R_1) represent the linear dispersive effect, while Q_n and R_n for $n \geq 2$ describe both resonant and nonresonant nonlinear wave interactions. This expansion can be considered as a generalization of Stokes' expansion for traveling waves to unsteady waves. It has been shown by Bateman *et al.*[2] that the resulting system can be also obtained by expanding the Dirichlet–Neumann operator, as suggested by Craig and Sulem.[5]

For example, the third-order system can be written explicitly in terms of ζ and Φ (Choi[44]) as

$$\frac{\partial \zeta}{\partial t} + \mathcal{L}[\Phi] + \nabla \cdot (\zeta \nabla \Phi) + \mathcal{L}[\zeta\mathcal{L}[\Phi]] + \nabla^2\left(\frac{1}{2}\zeta^2\mathcal{L}[\Phi]\right) + \mathcal{L}\left[\zeta\mathcal{L}[\zeta\mathcal{L}[\Phi]] + \frac{1}{2}\zeta^2\nabla^2\Phi\right] = 0, \tag{6}$$

$$\frac{\partial \Phi}{\partial t} + g\zeta + \frac{1}{2}\nabla\Phi \cdot \nabla\Phi - \frac{1}{2}(\mathcal{L}[\Phi])^2 - \mathcal{L}[\Phi](\zeta\nabla^2\Phi + \mathcal{L}[\zeta\mathcal{L}[\Phi]]) = 0, \tag{7}$$

where the linear operator $\mathcal{L}$ is defined as $\mathcal{L}[\Phi] = -\mathcal{F}^{-1}[k\tanh(kh)\mathcal{F}[\Phi]]$, where $\mathcal{F}$ and $\mathcal{F}^{-1}$ represent the Fourier and inverse Fourier transforms, respectively (see Appendix A). The system given by Eqs. (6) and (7) can be reduced to various asymptotic models for surface waves, including the NLS equation, the Boussinesq equations, the KdV equation, etc., by imposing appropriate approximations, as shown by Choi.[44]

System (1) possesses conservation laws for mass m, horizontal momentum $\boldsymbol{M}$, and total energy E,

$$m = \int_D \zeta \mathrm{d}\boldsymbol{x}, \quad \boldsymbol{M} = \int_D \zeta \nabla \Phi \mathrm{d}\boldsymbol{x},$$
$$E = \frac{1}{2}\int_D \left(\Phi \sum_{n=1}^{\infty} Q_n[\zeta,\Phi] + g\zeta^2\right)\mathrm{d}\boldsymbol{x}, \tag{8}$$

where D is the domain of interest. These conserved quantities are monitored when system (1) is solved numerically.

As a first step toward validating the pseudospectral model for broadband irregular waves, we consider long-crested waves in this paper and assume that the waves are independent of the transverse coordinate. To solve numerically the system given by Eq. (1), the infinite series on the right-hand sides of Eq. (1) are truncated up to the first Mth order nonlinear terms and the system is then integrated in time using a fourth-order Runge–Kutta scheme. The truncated right-hand sides of Eq. (1) are evaluated using a pseudospectral method based on fast Fourier transform, for which ζ and Φ are approximated by the following truncated Fourier series,

$$\zeta(x,t) = \sum_{n=-N/2+1}^{n=N/2} a_n(t)e^{ik_n x}, \quad \Phi(x,t) = \sum_{n=-N/2+1}^{n=N/2} b_n(t)e^{ik_n x}, \tag{9}$$

where N is the number of Fourier modes, $k_n = 2\pi n/L$, and L is the computational domain length. As in West *et al.*,[1] to reduce aliasing errors due to truncation of Fourier series, the number of Fourier modes is increased to $\tilde{N}$ in our computations, such that $\tilde{N} = (M+1)N/2$ and the Fourier coefficients beyond the first N Fourier modes are set to zero at each substep of the Runge–Kutta scheme. For the case of $M=2$, we recover the well-known "3/2-rule" and, for the third-order nonlinear computations with $M=3$, the number of Fourier modes is doubled although the number of the "physical" Fourier modes is just N. For numerical stability, the linear part of the system given by Eq. (1) is solved exactly using an integrating factor approach, as suggested by Craig and Sulem.[5] The number of Fourier modes is chosen to be $N = 1024$ in our computations. The accuracy of our numerical solutions is tested by monitoring conserved quantities: mass m, horizontal momentum M, and total energy E. For our numerical results for irregular waves presented in this paper, these quantities are conserved typically up to a relative error of $O(10^{-10})$ with a time step of $\Delta t/T_p = 0.02$, where T_p is the peak wave period. No significant changes in conserved quantities have been observed for smaller time steps.

B. Modified nonlinear Schrödinger equation

If one considers unidirectional waves of small steepness characterized by a narrow-band spectrum centered at frequency ω_p, the surface elevation ζ can be expanded as

$$\zeta(x,t) = \bar{\zeta} + \frac{1}{2}(A_1 e^{\mathrm{i}(k_p x - \omega_p t)} + A_2 e^{2\mathrm{i}(k_p x - \omega_p t)} + A_3 e^{3\mathrm{i}(k_p x - \omega_p t)} + \cdots + C.C.), \tag{10}$$

where $C.C.$ denotes the complex conjugate. In Eq. (10), $\bar{\zeta}$ and A_n are the mean surface elevation and the complex amplitudes of the nth harmonic, respectively, and are assumed to vary slowly in space and time. If the bandwidth of the spectrum is small, or, more specifically, $O(\epsilon)$, the complex amplitude $A \equiv A_1$ is governed, for infinitely deep-water, by the MNLS correct to $O(\epsilon^4)$ (Trulsen and Stansberg[29] and Kit and Shemer[45]),

$$\frac{\partial A}{\partial x}+\frac{2k_p}{\omega_p}\frac{\partial A}{\partial t}+\mathrm{i}\frac{k_p}{\omega_p^2}\frac{\partial^2 A}{\partial t^2}+\mathrm{i}k_p^3|A|^2A - \frac{k_p^3}{\omega_p}\left(6|A|^2\frac{\partial A}{\partial t}+2A\frac{\partial |A|^2}{\partial t}-2\mathrm{i}A\mathcal{H}\left[\frac{\partial |A|^2}{\partial t}\right]\right)=0, \tag{11}$$

where $\mathcal{H}$ is the Hilbert transform defined by $\mathcal{H}[f]=(1/\pi)\int_{-\infty}^{\infty}f(\xi)/(\xi-t)d\xi$. When the last three terms are neglected, the NLS equation is recovered. Since we are interested in the comparison of numerical solutions of the MNLS equation with surface elevation measurements at different wave probe locations, the MNLS equation is written as a spatial evolution equation. Once Eq. (11) is solved numerically to compute the complex amplitude A, the surface elevation ζ can be reconstructed from Eq. (10), where the higher-order corrections $\bar{\zeta}$, A_2, and A_3 are given (Trulsen and Stansberg[29]) by

$$\bar{\zeta}=\frac{k_p}{2\omega_p}\mathcal{H}\left[\frac{\partial |A|^2}{\partial t}\right],\quad A_2=\frac{k_p}{2}A^2+\mathrm{i}\frac{k_p^2}{\omega_p}A\frac{\partial A}{\partial t},\quad A_3=\frac{3k_p^2}{8}A^3. \tag{12}$$

It should be emphasized that the reconstruction of the surface elevation without the higher-order corrections in Eq. (12) shows poor comparison with our laboratory measurements.

Spatial evolution equation (11) for A is solved using a pseudospectral method in time with the number of Fourier modes of $N=512$ combined with a fourth-order Runge–Kutta integration scheme in space with $\Delta x/\lambda_p=1.6\times 10^{-4}$ with λ_p being the peak wavelength. In Fourier space, the Hilbert transform can be easily computed by $\mathcal{F}(\mathcal{H}[f])=\mathrm{i}\,\mathrm{sign}(f)\mathcal{F}(f)$. The accuracy of the numerical solution is measured by monitoring conservation of an energylike quantity $\int|A|^2\mathrm{d}t$ which has a relative error of $O(10^{-12})$ in our computations.

III. LABORATORY EXPERIMENTS

A. Wave characteristics

A series of laboratory experiments were conducted in a rectangular wave basin at the Institute for Ocean Technology in Newfoundland, Canada. The basin is 75 m long, 32 m wide, and has a water depth of 2.5 m. The finite depth effect is found to be negligible for the waves considered in our experiments and the infinite depth ($h\to\infty$) limit is considered to solve the PS model. Piston-type wavemakers present on two adjacent walls of the basin can generate both unidirectional and multidirectional waves of any wave spectrum. Each segmented wavemaker is 2 m high and 0.5 m wide. On the two opposite sides, passive wave absorbers made of expanded metal sheets with varying porosities and spacings prevent any waves to reflect back to the wave basin. The surface elevation was measured using 20 wave probes of capacitance type equally spaced by 1.2 m with a sampling rate of 0.02 s (50 Hz) and time series over 500 s were recorded for our experiments. All the data were acquired using GDAC (GEDAP Data Acquisition and Control) client-server acquisition system, developed by National Research Council Canada, Institute for Ocean Technology.

To generate irregular waves, a random phase normally distributed over the range between 0 and 2π is introduced to the wavemaker whose motion was characterized by the JONSWAP spectrum,

$$S_\omega(\omega)=\frac{5}{16}\frac{\omega_p^4H_s^2}{\omega^5}\exp\left[-\frac{5}{4}\left(\frac{\omega_p}{\omega}\right)^4\right]\gamma^{\exp[-(\omega-\omega_p)^2/2\sigma^2\omega_p^2]}, \tag{13}$$

where H_s is the significant wave height, γ is the peak enhancement factor, ω_p is the peak frequency, and σ is a function of wave frequency defined by $\sigma=0.07$ for $\omega\le\omega_p$, while $\sigma=0.09$ for $\omega>\omega_p$. In our experiments, we fixed the significant wave height H_s and the peak frequency f_p to be $H_s=0.1$ m and $f_p=\omega_p/(2\pi)=1$ Hz, respectively, but we considered two different values of the peak enhancement factor: $\gamma=3.3$ and $\gamma=20$. Additionally, a low-pass filter with a cutoff frequency of 1.2 Hz was applied at the wavemaker to generate a nonequilibrium wave spectrum and the higher frequency components were therefore excited by nonlinearity as the waves propagate downstream. From the linear dispersion relation given by $k_p=4\pi^2f_p^2/g$, the peak wave number k_p corresponding to the peak wave frequency $f_p=1$ Hz is given by $k_p=4.03$ m^{-1}. Therefore, the peak wavelength is $\lambda_p=2\pi/k_p=1.56$ m.

In this paper, as mentioned previously, we consider only long-crested waves propagating in the x-direction and the wave probes are aligned with the wave propagation direction over a distance of 22.8 m. Since the width of the basin is large compared with the characteristic wavelength in our experiments, viscous energy dissipation that occurs mostly on sidewalls is assumed to be negligible at the center of the basin where our wave probes are located. The first wave probe that is our probe of reference is 17.8 m away from the wavemaker (equivalent to 11.4 peak wavelengths) and the waves measured even at the first wave probe are fully developed and nonlinear. To test their applicability in describing the evolution of nonlinear random wave fields, we initialize the two wave models (the PS and MNLS models) using measurements at the first probe and examine how accurately these models predict the surface elevation at other probe locations downstream.

There are two important physical parameters that characterize the evolution of irregular waves: the characteristic wave steepness and the bandwidth. When the characteristic wave steepness is estimated by $\epsilon_p=k_pH_s/2$, it is found to be $\epsilon_p=0.201$ [or $H_s/(2\lambda_p)=0.032$] for $H_s=0.1$ m. Notice that these waves can no longer be considered linear and the wave steepness could be locally much larger than this estimate. As can be seen later, even the weakly nonlinear assumption is inapplicable. The effect of the spectral bandwidth is examined by choosing two different peak enhancement factors: $\gamma=3.3$ and $\gamma=20$. For example, when Δf is defined as half the spectrum width at the half peak amplitude of the theoretical JONSWAP spectrum, its dependence on γ is found to be $\triangle f/f_p=0.095$ and 0.056 for $\gamma=3.3$ and $\gamma=20$, respectively.

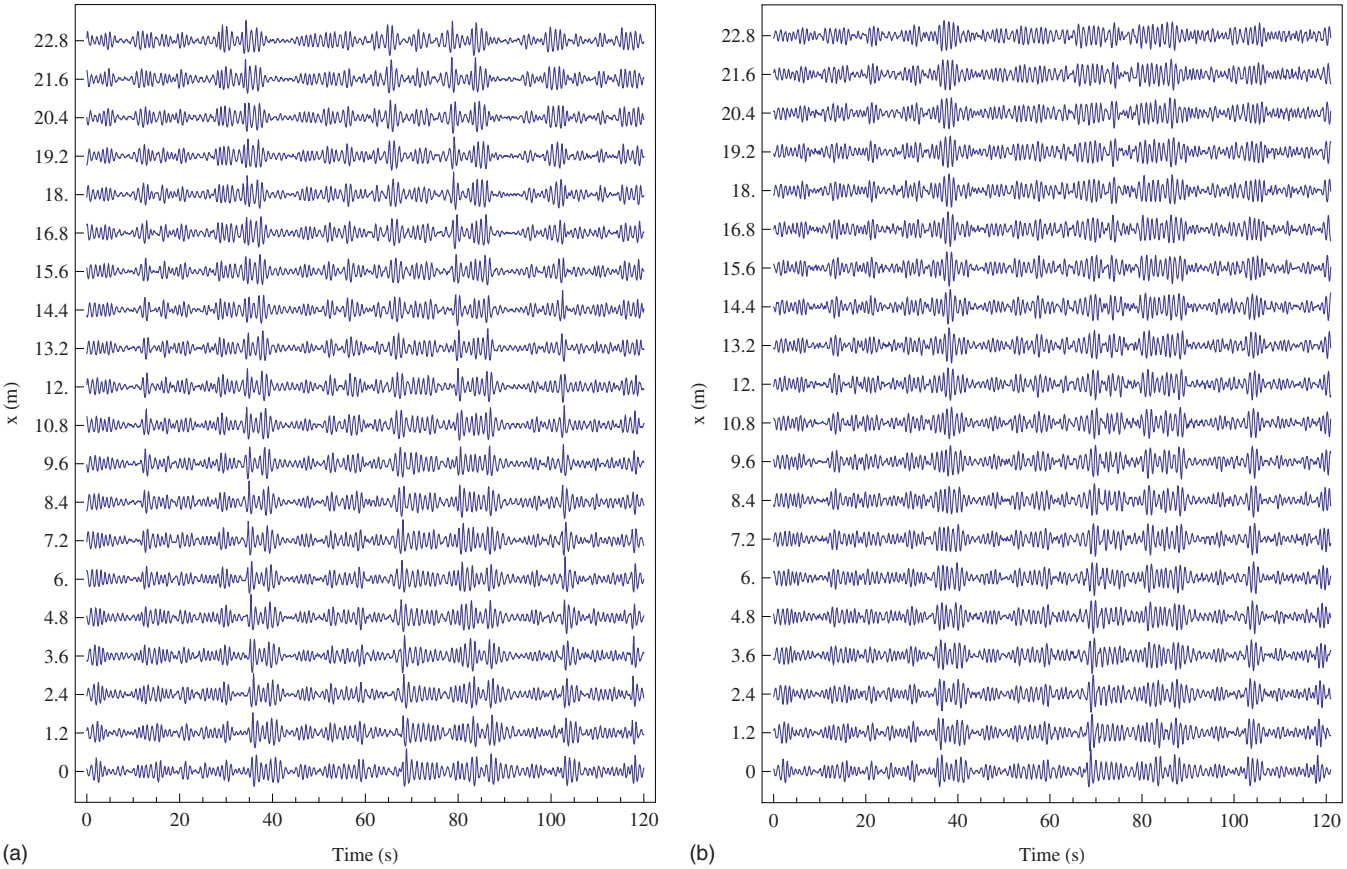

FIG. 1. (Color online) Evolution of the wave field characterized by the JONSWAP spectrum with $H_s=0.1$ m and $\gamma=3.3$ in a reference frame moving with the group velocity based on the peak frequency C_{g_p}: (a) Experimental measurements; (b) linear theory based on the first probe measurement.

From the Benjamin–Feir theory[46] for Stokes waves, it is well-known that the ratio of the wave steepness to the frequency difference between a carrier wave and its perturbation, which measures the nonlinear and dispersive effects of wave groups, respectively, has to be greater than a critical value for modulational instability to occur. A similar measure called the Benjamin–Feir index β has been also introduced for irregular waves (Alber,[47] Crawford *et al.*,[48] and Janssen[49]) as

$$\beta = \frac{\epsilon_p}{(\sqrt{2}\Delta f/f_p)}, \tag{14}$$

where Δf is the spectral bandwidth. Beyond the critical Benjamin–Feir index known to be $\beta_{\text{crit}}=1$, an irregular wave field is expected to be unstable so that wave focusing could occur. The wave field becomes more unstable as its bandwidth decreases or its steepness increases. In our experiments, the Benjamin–Feir indices are $\beta=1.49$ for $\gamma=3.3$ and $\beta=2.25$ for $\gamma=20$. Therefore, wave focusing due to modulational instability is expected to occur more strongly for the case of $\gamma=20$.

We should point out that the Benjamin–Feir index and the wave steepness in our study are larger than those considered in previous studies including, for example, Onorato *et al.*[42] and Janssen,[49] where the Benjamin–Feir indices were less than 2. Therefore, stronger modulational instability is expected to occur in our experiments, which suggests the development of a more "rogue sea" state with the possible occurrence of wave breaking. Since the waves in our experiments fall locally into a strongly nonlinear wave regime, the cubic nonlinear Schrödinger equation compares poorly with our experiments and, instead, the MNLS equation is adopted in addition to the PS model. Considering that the time scale of the modulational instability normalized with respect to the peak wave period is $O(\epsilon_p^{-2})$ and the group velocity corresponding to the peak frequency is $C_{g_p}=g/(2\omega_p)\approx 0.78$ m/s, the distance over which the modulational instability is expected to appear should be O (24 m). Since the distance between the first and last wave probes is 22.8 m (about 14 peak wavelengths), modulational instability is expected to be observed in our experiments.

B. Observation

We first consider the spatial evolution of the surface elevation for the case of $\gamma=3.3$ and examine how wave groups evolve as they propagate downstream. As shown in Fig. 1(a), we choose a time series of 120 s long at the first wave probe in which a number of wave groups are identified. Notice that we follow the wave groups with the group velocity based on the peak frequency $C_{g_p}\approx 0.78$ m/s. It is interesting to notice that most wave groups propagate approximately with the peak group velocity although some wave groups move slightly faster.

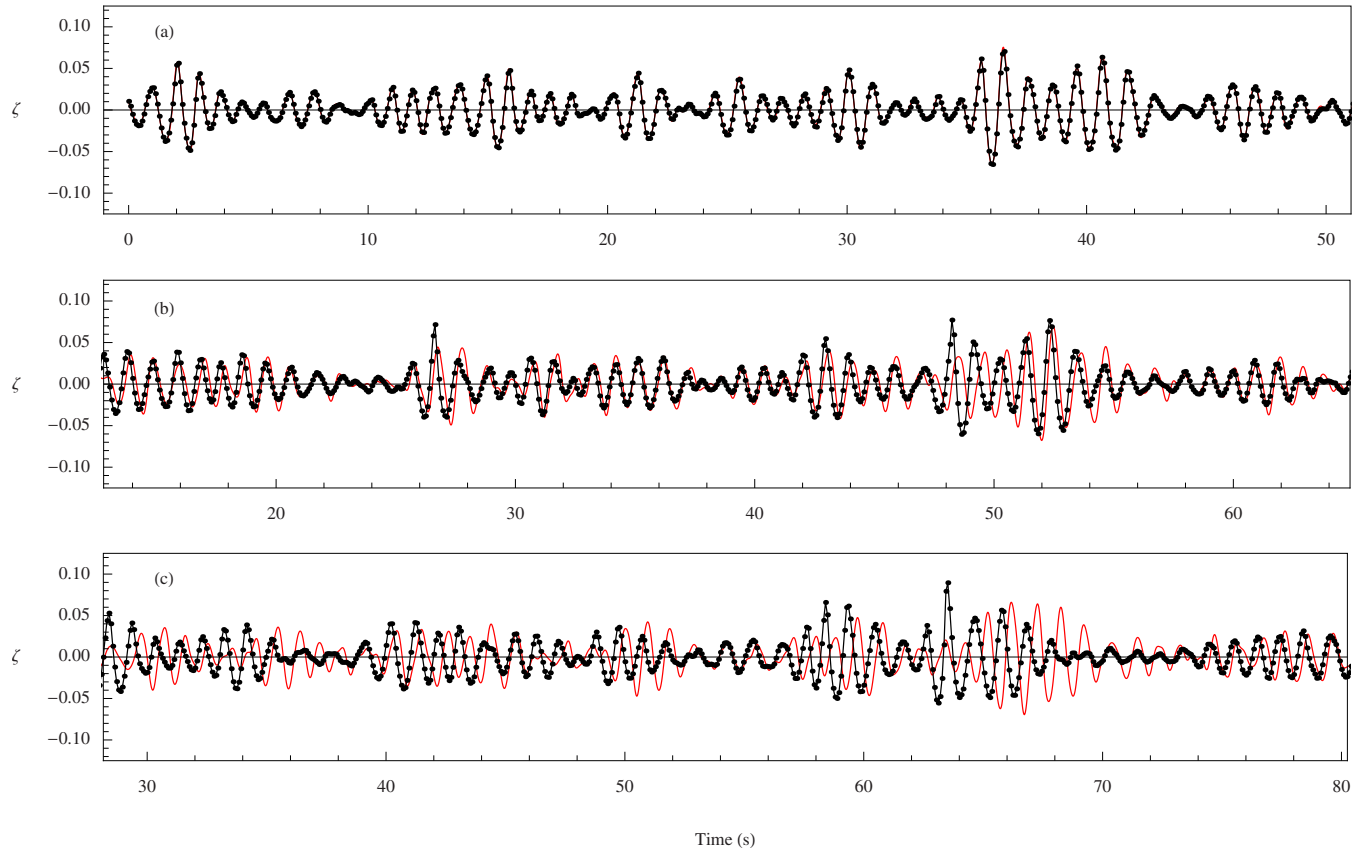

FIG. 2. (Color online) Comparison of the surface elevation with $H_s=0.1$ m and $\gamma=3.3$ between experimental measurements (dot-line) and numerical solutions of the linear model (solid line) at $x=0$ m, $x=10.8$ m, and $x=22.8$ m (from top to bottom).

Due to nonlinearity and dispersion, the wave groups evolve continuously in space and sometimes interact with each other. Over the distance where our wave probe measurements are available (which correspond approximately to 14 peak wavelengths), almost one cycle of focusing-defocusing process is observed, for example, for the wave group that appears around $t=105$ s at the first probe. Wave focusing results in large wave slope and often leads to wave breaking, which is difficult to model numerically. When no wave breaking occurs, this focusing-defocusing process might recur, as observed in Stokes waves with small sideband perturbations although it is not clear if this phenomenon is still observable in irregular wave fields. We will look more closely at the evolution of steep wave groups in Sec. IV where our measurements are compared with numerical solutions.

To examine how nonlinear our wave groups are, the numerical solution of the linear model with $M=1$ is shown in Fig. 1(b) by initializing the model with the experimental measurement at the first probe, such that the linear solution matches with the measurement at the first wave probe (see Sec. IV A, for a detailed description of the model initialization). We can see clearly that, under linear wave theory, wave groups show little focusing and are often broadened due to dispersion. We also notice that the linear wave groups propagate at a speed slower than the group velocity based on the peak frequency. For clarity, a more detailed comparison between the linear solution and our experimental measurement for the wave group observed for the first 50 s is given in Fig. 2 at three different probe locations: $x=0$, 10.8, and 22.8 m (corresponding to 0, 6.92, and 14.62 peak wavelengths away from the first probe). The linear solution at $x=10.8$ m ($x/\lambda_p \simeq 6.92$) starts to deviate from our measurement and fails to capture the focused peak observed around $t=64$ s at the last wave probe located at $x=22.8$ m ($x/\lambda_p \simeq 14.62$). Therefore, we can conclude that our wave fields are truly nonlinear, as discussed in Sec. III A.

For the case of $\gamma=20$, similar conclusions can be drawn, but stronger wave focusing is observed experimentally, as shown in Fig. 3(a). The linear solution is considerably different from measurements at downstream probes. For example, see the evolution of the wave group around $t=85$ s at the first probe. We also remark that the local maximum amplitude of the wave envelope for $\gamma=20$ becomes much greater than that for $\gamma=3.3$ although the significant wave heights are the same. This can be understood from the fact that the bandwidth for $\gamma=20$ is smaller than that for $\gamma=3.3$, leading to a larger Benjamin–Feir index for $\gamma=20$. Thus, focusing due to modulational instability is enhanced for $\gamma=20$, as discussed in Sec. III A.

In what follows, we will compare our numerical solutions of the PS model and the MNLS equation with experimental measurements and examine their capability in predicting nonlinear irregular wave fields not only in wave amplitude but also in phase.

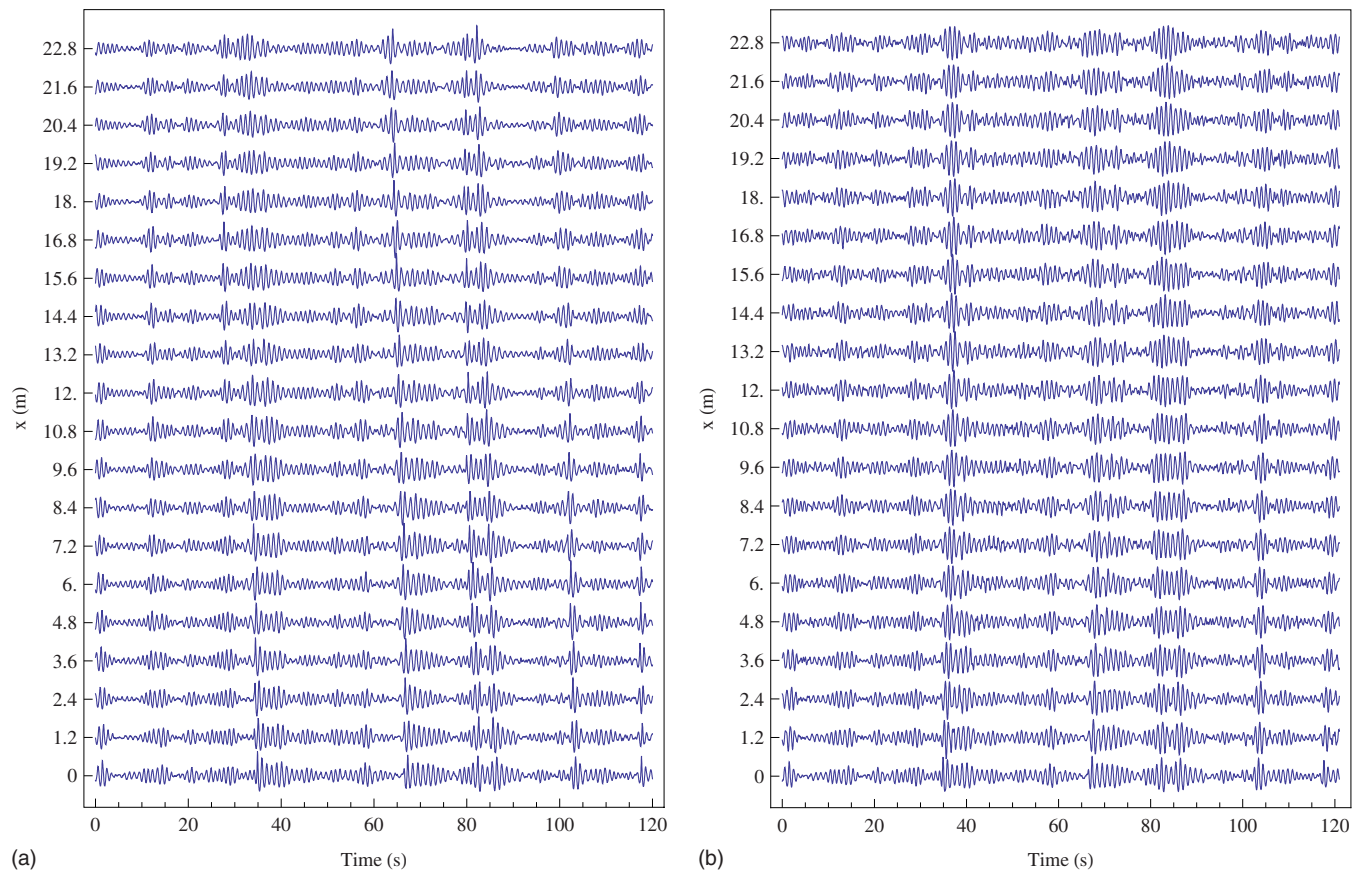

FIG. 3. (Color online) Evolution of the wave field characterized with the JONSWAP spectrum with $H_s=0.1$ m and $\gamma=20$ in a reference frame moving with speed the group velocity based on the peak frequency, C_{g_p}: (a) Experimental measurements; (b) linear theory based on the first probe measurement.

IV. NUMERICAL SOLUTIONS

A. Initialization

Before presenting our numerical solutions compared with laboratory experiments, we outline the procedure to initialize the wave models.

Since we have only point measurements of the surface elevation (as a function of time) at 20 different locations, it is not straightforward to initialize the PS model which requires initially the surface elevation and the velocity potential fields in the entire computational domain. When we denote by $\zeta_1(t)$ a time history of the surface displacement at the first probe which without loss of generality is assumed to be located at $x=0$, the surface elevation and the velocity potential can be expressed, based on linear theory, as a linear superposition of sinusoidal waves propagating in the x-direction,

$$\zeta(x,t) = \sum_n a_n e^{\mathrm{i}(k_n x - \omega_n t)} + C.C.,$$
$$\Phi(x,t) = \sum_n c_n e^{\mathrm{i}(k_n x - \omega_n t)} + C.C., \tag{15}$$

where $\omega_n = 2\pi n/T$ with T being the total time interval for $\zeta_1(t)$ and the wave numbers k_n are computed using the deep-water linear dispersion relation, $k_n = \omega_n^2/g$. The coefficients a_n in Eq. (15) with $x=0$ are found from the Fourier expansion of $\zeta_1(t)$, $\zeta_1(t) = \Sigma a_n \exp(-\mathrm{i}\omega_n t)$, obtained from the surface elevation measurement over 120 s with a sampling rate of 0.02 s. An alternative way to generate $\zeta_1(t)$ at $x=0$ is to use an oscillating pressure, as in Smith[8] where a similar set of equations is solved for water of finite depth with bottom topography.

On the other hand, c_n is found from the linear relationship between ζ and Φ, which yields $c_n = -i(\omega_n/k_n)a_n$. Then, we initialize the PS model by evaluating Eq. (15) at $t=0$ and solve evolution equations (1) by decomposing the computational domain into two regions: the linear and nonlinear regions. In the first region upstream of the first probe, the linear equations ($M=1$) are solved so that the waves reaching the first probe match exactly with experimental measurements at the first probe, whereas the nonlinear equations with $M>1$ are solved in the second region which is downstream of the first probe. Thus, the waves beyond the first probe propagate nonlinearly. This is implemented simply by multiplying the nonlinear terms in evolution equations (1) by a smooth Heaviside-like function varying from 0 to 1. The width of the transition region centered at the first probe is about 2 grid points. At the downstream probe locations, our numerical solutions of the PS model for the surface elevation are recorded as time series and are compared with laboratory measurements.

With this initialization scheme, our numerical solutions for the surface elevation match with experimental measure-

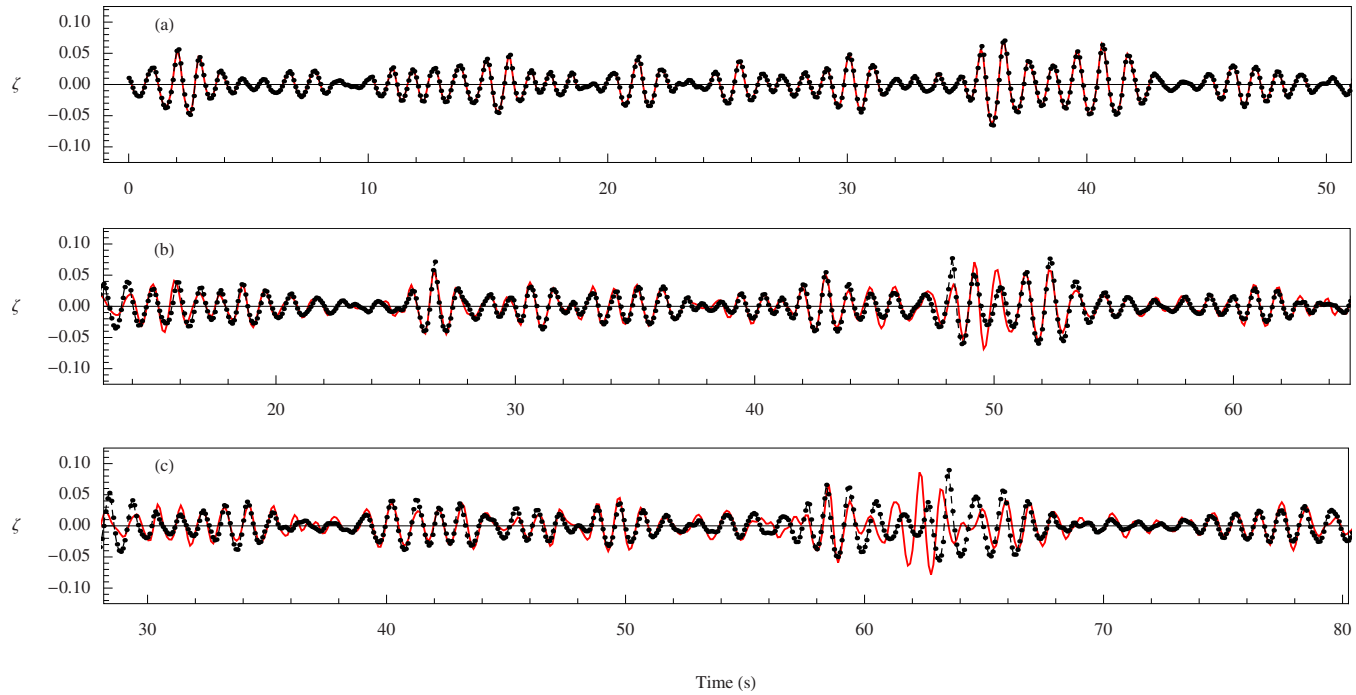

FIG. 4. (Color online) Comparison for the surface elevation with $H_s=0.1$ m and $\gamma=3.3$ between experimental measurements (dots) and numerical solutions of the MNLS equation (solid line) at $x=0$ m, $x=10.8$ m, and $x=22.8$ m (from top to bottom).

ments at the first probe, but the velocity potential (therefore, the fluid velocity) might be inaccurate since we use the linear relationship between the free surface elevation and the velocity potential to initialize the velocity potential. This error could result in some discrepancy between numerical solutions and experimental measurements at downstream probe locations, but is found small, as can be seen later. This could be explained by the fact that the linear velocity potential is valid up to the third-order in Stokes expansion for infinitely deep-water waves.

On the other hand, since the MNLS equation for $A(x,t)$ is written as a spatial evolution equation, it should be straightforward to initialize A from a time history of the surface elevation measured at the first wave probe, but it is found that A has to be initialized with care. In order to find the envelope of $\zeta_1(t)$, we compute the following complex quantity: $\zeta_1(t)+i\mathcal{H}[\zeta_1(t)]=\rho(t)e^{i\theta(t)}$ and, from Eq. (10) without the higher-order corrections, initialize the complex amplitude A as $A(0,t)=\rho e^{i(\theta+\omega_p t)}$. Once the numerical solution of the MNLS equation for $A(x,t)$ is obtained, the surface elevation is reconstructed using Eq. (10) with the higher-order corrections. Without the higher-order correction terms, poor agreement between numerical solutions and experimental measurements is observed at downstream probe locations. On the other hand, with the higher-order correction terms, the reconstructed surface elevation at the first probe location, $\zeta(0,t)$, will not match with the original time series $\zeta_1(t)$ since any higher-order corrections in Eq. (10) have been neglected in initializing A. To overcome this difficulty, we initialize A by applying to $A(0,t)$ a low-pass filter with cutoff frequency whose value is increased from $3\omega_p$ until a reasonable correlation (99% or better) between $\zeta_1(t)$ and $\zeta(0,t)$ is obtained. With this initialization technique, the numerical solutions of the MNLS equation are found to agree reasonably well with laboratory experiments over a certain distance, as discussed later.

B. Numerical solutions compared with laboratory experiments

Now we present our numerical solutions of the MNLS equation and the PS model and their comparison with experimental measurements for the surface elevation at 20 wave probes spanning 22.8 m (about 14 peak wavelengths). In particular, we focus on the spatial evolution of wave groups over a time window of about 120 s in which large peaks due to wave focusing are found to form. We should point out that the MNLS equation should be of limited success in describing the evolution of strongly nonlinear wave groups since the weakly nonlinear and small-bandwidth assumptions in deriving the MNLS equation might not be applicable here. To follow the same wave groups, the time window is shifted, at downstream probe locations, according to the group velocity based on the peak frequency, $C_{g_p}\simeq 0.78$ m/s.

1. $\gamma=3.3$

For the case of $\gamma=3.3$, while its numerical solutions show good agreement with our experimental measurements for relatively small wave groups, the MNLS equation fails to describe large wave groups at the 10th and 20th wave probes located at $x=10.8$ m and $x=22.8$ m (which correspond to $x/\lambda_p\simeq 6.92$ and $x/\lambda_p\simeq 14.62$, respectively), as shown in Fig. 4. At $x=10.8$ m, a major discrepancy between the numerical and experimental results appears in the wave group around $t=50$ when the largest peak forms. At the last probe (at $x/\lambda_p\simeq 14.62$), the MNLS equation predicts poorly this

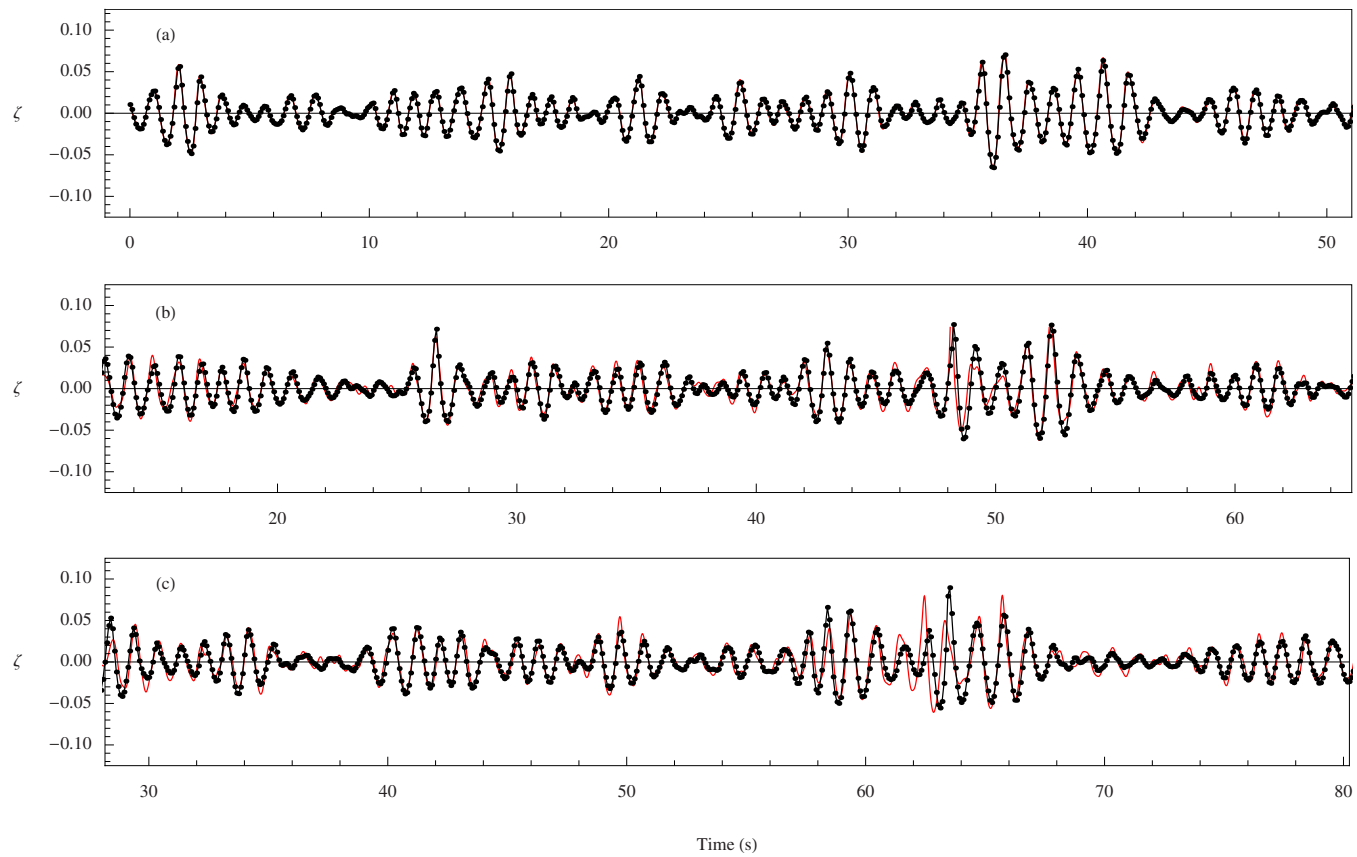

FIG. 5. (Color online) Comparison for the surface elevation with $H_s=0.1$ m and $\gamma=3.3$ between experimental measurements (dots) and numerical solutions of the third-order nonlinear model (solid line) at $x=0$ m, $x=10.8$ m, and $x=22.8$ m (from top to bottom).

strongly nonlinear wave group observed over a period of 56 s$<t<$70 s. The phase error between the measured and computed times when the largest peak is formed is about 2 s (two wave periods) at the last wave probe location. Notice that the largest peak corresponds to the crest of the envelope of the wave group and is expected to move with the group velocity. This implies that the error in the average group velocity is about 6.8% from $\Delta C_g/C_{gp}=C_{gp}\Delta t/L$, where ΔC_g and Δt are the group velocity and phase errors, respectively, while L is the distance between the first and last wave probes. We remark that this comparison is based on our initialization scheme for A to incorporate the higher-order nonlinear corrections when the surface elevation ζ is reconstructed. Otherwise, the comparison between numerical solutions of the MNLS equation and laboratory experiments is worse than what we presented here. In addition, the NLS equation shows poor comparison with laboratory experiments and, therefore, its solutions are not presented here.

Our results agree with the previous work of Trulsen and Stansberg[29] where validity of the NLS and MNLS equations is examined with laboratory experiments on bichromatic waves. It is suggested that the range of validity of these weakly nonlinear models in terms of the propagation distance depends on the wave steepness. For example, when the dimensionless distance is defined by $\eta=\epsilon^2 k_c x$, where ϵ and k_c are the wave steepness and the center frequency, respectively, Trulsen and Stansberg[29] claimed that the range of validity is $\eta=1$ for the NLS model as well as the linear model and $\eta=3$ for the MNLS model. Beyond $\eta=5$, neither NLS nor MNLS model is found reliable. Although this conclusion is for regular waves, we notice that our numerical solutions of the MNLS equation start to deviate from laboratory measurements at the last probe located at $x=22.8$ m which is equivalent to $\eta=3.71$ with $k_p=4.02$ and $\epsilon_p=0.201$.

Now we compare in Fig. 5 the numerical solution of the third-order PS model ($M=3$) with experimental measurements. At two downstream probe locations (at $x=10.8$ m and $x=22.8$ m), our numerical solution of the third-order model, in general, agrees better with experimental measurements than that of the MNLS equation in both wave amplitude and phase.

However, some discrepancy still exists at the last wave probe over 10 s between 58 s and 68 s during which the largest wave group is observed. This indicates that third-order nonlinearity might be insufficient and a higher-order nonlinear model needs to be used. In order to clarify a source of this discrepancy, the fifth- and seventh-order ($M=5$ and 7, respectively) PS models are solved numerically. In Fig. 6, we follow the largest wave group with C_{g_p} at five different probe locations ($x=0$, 4.8, 10.8, 16.8, and 22.8 m away from the first probe) and show close-up views of the numerical solutions of the third-, fifth-, and seventh-order PS models compared with experimental measurements. Notice that a large peak is observed around $t=41.5$ s from a time series measured at $x=4.8$ m ($x/\lambda_p\simeq 3.08$) and the third-order model

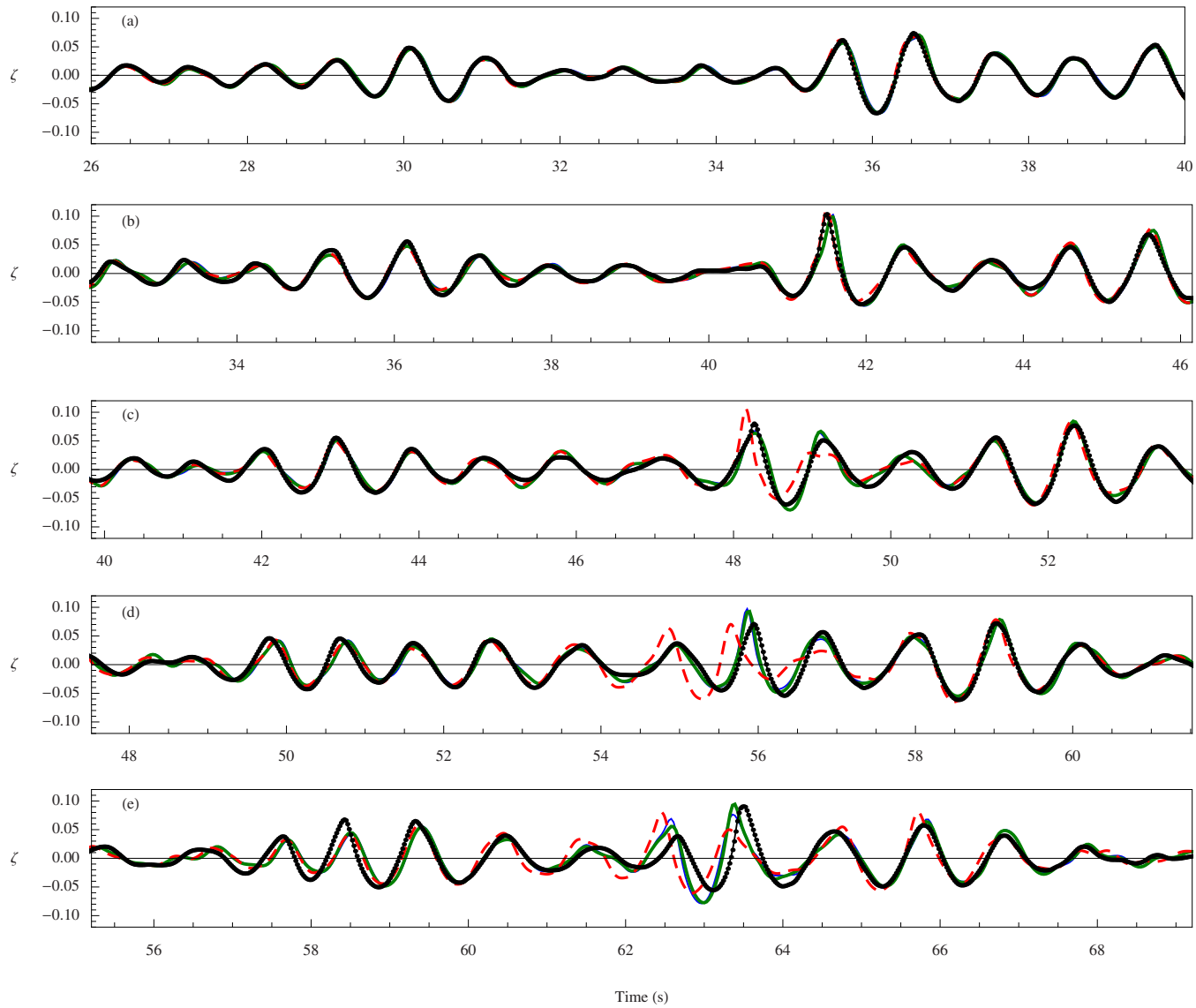

FIG. 6. (Color online) Comparison for the surface elevation with $H_s=0.1$ m and $\gamma=3.3$ between experimental measurements (dotted line) with numerical solutions of the third-order (dashed line), fifth-order (thick solid line), and seventh-order (thin solid line) PS models at $x=0$ m, $x=4.8$ m, $x=10.8$ m, $x=16.8$ m, and $x=22.8$ m (from top to bottom).

starts to deviate from our experimental measurements at $x=10.8$ m ($x/\lambda_p \simeq 6.92$) when a large peak is observed around $t=48$ s. Beyond this wave probe, the third-order PS model fails to follow the crest of this wave group. However, the higher-order numerical solutions are still in good agreement with experimental measurements up to $x=16.8$ m ($x/\lambda_p \simeq 10.77$). At the last wave probe located at $x=22.8$ m ($x/\lambda_p \simeq 14.62$), in terms of the instant when the largest peak is observed, a small phase error of approximately 0.25 s (a quarter peak wave period) is observed between the fifth-order solution and experimental measurements. Notice that, compared with experimental measurements, the numerical solutions seem to overestimate the local wave amplitude when focusing occurs, which results in a phase shift at downstream probe locations. We remark that the difference between the fifth- and seventh-order solutions is quite small and is hardly noticeable in Fig. 6. This implies that a source of this small discrepancy is not the order of nonlinearity, but should be attributed to other causes, such as, for example, uncertainty in initializing the velocity potential, viscous effects, and, most importantly, weak three-dimensionality observed in our experiments.

From our comparison of numerical solutions with laboratory experiments, it can be concluded that the fifth-order PS model accurately predicts the location and time of the occurrence of large wave peaks. The comparison between the numerical solution of the fifth-order PS model and laboratory measurements at all 20 probes is shown in Fig. 7.

To examine the evolution of these wave groups over a much longer distance (beyond 22.8 m), we solve the fifth-order PS model in a computational domain of 200 m (130 peak wavelengths), as shown in Fig. 8. Since the wave groups propagate over a large distance, we have to follow them with the group velocity with a leading-order nonlinear correction, which is given by $C_{g_p}=\frac{1}{2}(g/k_p)^{1/2}[1$

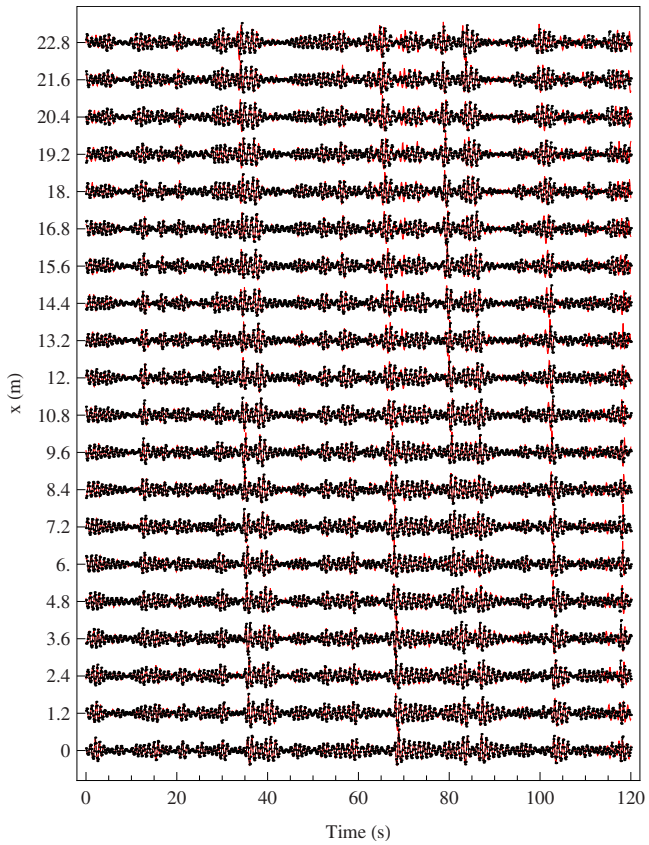

FIG. 7. (Color online) Evolution of the wave field characterized by the JONSWAP spectrum with $H_s=0.1$ m and $\gamma=3.3$ in a reference frame moving with the group velocity based on the peak frequency C_{g_p}: Experimental measurements (dots) compared with numerical solutions of the fifth-order PS model (solid lines).

$+\frac{5}{2}k_p^2(H_s/2)^2+\cdots]\approx 0.85$ from kinematic consideration of $C_{g_p}=\mathrm{d}\omega/\mathrm{d}k$. A number of wave groups of different amplitudes can be identified at the first probe from a density plot in Fig. 8(a). We notice that different wave groups travel with different speeds and interact as they propagate downstream. To better illustrate the dynamics of these wave groups, the detailed evolution of wave envelopes is shown in Fig. 8(b) for wave groups observed at the first wave probe for 0 s $\leq t \leq 50$ s and $90 \leq t \leq 110$. The spatial evolution of the largest peak observed around $t=36$ s is complicated due to its interaction with neighboring wave groups, but the recurrence of wave focusing is obvious. A rather isolated wave group around $t=105$ s shows clearly the recurrence of the focusing-defocusing process, as evidenced in Fig. 8(c), which has been reported previously for regular waves with sideband perturbations.

2. $\gamma=20$

For the case of $\gamma=20$, as mentioned previously, the Benjamin–Feir index is large ($\beta=2.25$) and, as a consequence, stronger wave focusing is observed. For example, in Fig. 1, steep waves are recorded during a time period of 34 s$<t<$42 s at the first probe. Therefore, the MNLS equation is not expected to show good agreement with experimental measurements although the small-bandwidth assumption should be more relevant to $\gamma=20$ than $\gamma=3.3$. In fact, the formation of the largest wave group is not captured correctly by the MNLS equation, as shown in Fig. 9.

When the third-order PS model is solved, Fig. 10 shows the third-order solution compare reasonably well with laboratory measurements at the tenth wave probe located at $x=10.8$ m ($x/\lambda_p \simeq 6.92$), except for the largest wave group centered at $t \simeq 47$ s. Compared with the case of $\gamma=3.3$, the difference between numerical solution and laboratory measurement at the tenth probe is relatively large; in fact, the numerical solution overestimates the amplitude of the highest peak. Similar observations can be made at the last probe where the difference is more pronounced. It is interesting to notice that the MNLS equation seems to perform as good as the third-order PS model.

As shown in Fig. 11, even though the fifth-order PS model is solved, little improvement is achieved, which is different from the case for $\gamma=3.3$. This indicates that the order of nonlinearity is not a major cause of discrepancy for the case of $\gamma=20$. In fact, our numerical solutions show the emergence of very steep waves at the fifth probe, as can be seen at $x=4.8$ m around $t \simeq 40.75$ s. Since this particular wave is so steep, a higher-order computation seems to be necessary, but we should point out that a seventh-order computation failed, which usually indicates wave breaking, as shown by Tian *et al.*[15] Experimentally, for the case of $\gamma=20$, combined spilling/plunging wave breaking has been observed sporadically although its exact locations and times were not recorded. Therefore, the discrepancy between numerical solutions and experiment measurements should be attributed to multiple wave breaking that occurs between the first and tenth probes, which also introduces non-negligible three-dimensionality, but more detailed experiments might be necessary to make any further conclusion.

V. CONCLUDING REMARKS

Two mathematical models for nonlinear surface waves, the PS model and the MNLS equation, are adopted to test their applicability in describing the evolution of nonlinear irregular wave fields and their numerical solutions are compared with laboratory experiments in which strong focusing of wave groups and their interactions are observed. It is found that the third-order PS model is, in general, reliable in predicting the evolution of nonlinear wave groups, but, when strong focusing occurs, a higher-order PS model such as the fifth-order model should be used. On the other hand, the MNLS model could be an effective model when it is initialized appropriately, but its validity is found limited to weakly nonlinear, narrow-band wave fields, as expected.

It is confirmed both experimentally and numerically that the Benjamin–Feir index defined by a ratio between wave steepness and bandwidth proposed by Alber,[47] Crawford *et al.*,[48] and Janssen[49] is a good indicator of wave focusing events in irregular wave fields.

Based on our results for long-crested waves, the PS model is expected to describe the evolution of short-crested waves well. Although the PS model has been used to study the development of statistical properties of short-crested waves, it has not been fully validated, in terms of the ampli-

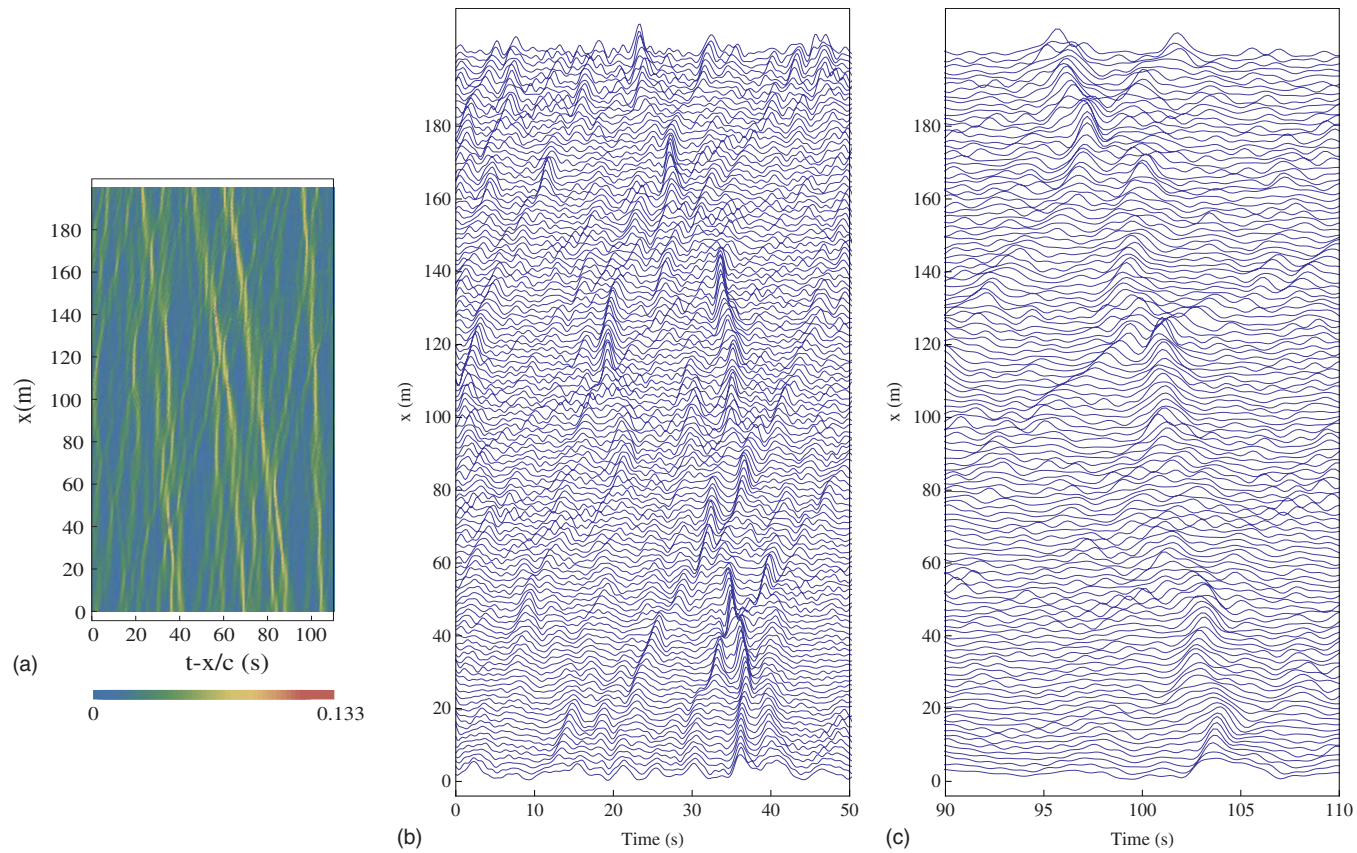

FIG. 8. (Color online) Numerical solution of the fifth-order PS model for the long-range evolution of a surface wave field initialized with the JONSWAP spectrum with $\gamma=3.3$: (a) Density plot for the amplitude of the wave envelope which shows clearly the propagation and interaction of wave groups for $0\ \mathrm{s} \leq t \leq 110\ \mathrm{s}$; (b) evolution of the wave envelope for $0\ \mathrm{s} \leq t \leq 50\ \mathrm{s}$; (c) evolution of the wave envelope for $90\ \mathrm{s} \leq t \leq 110\ \mathrm{s}$.

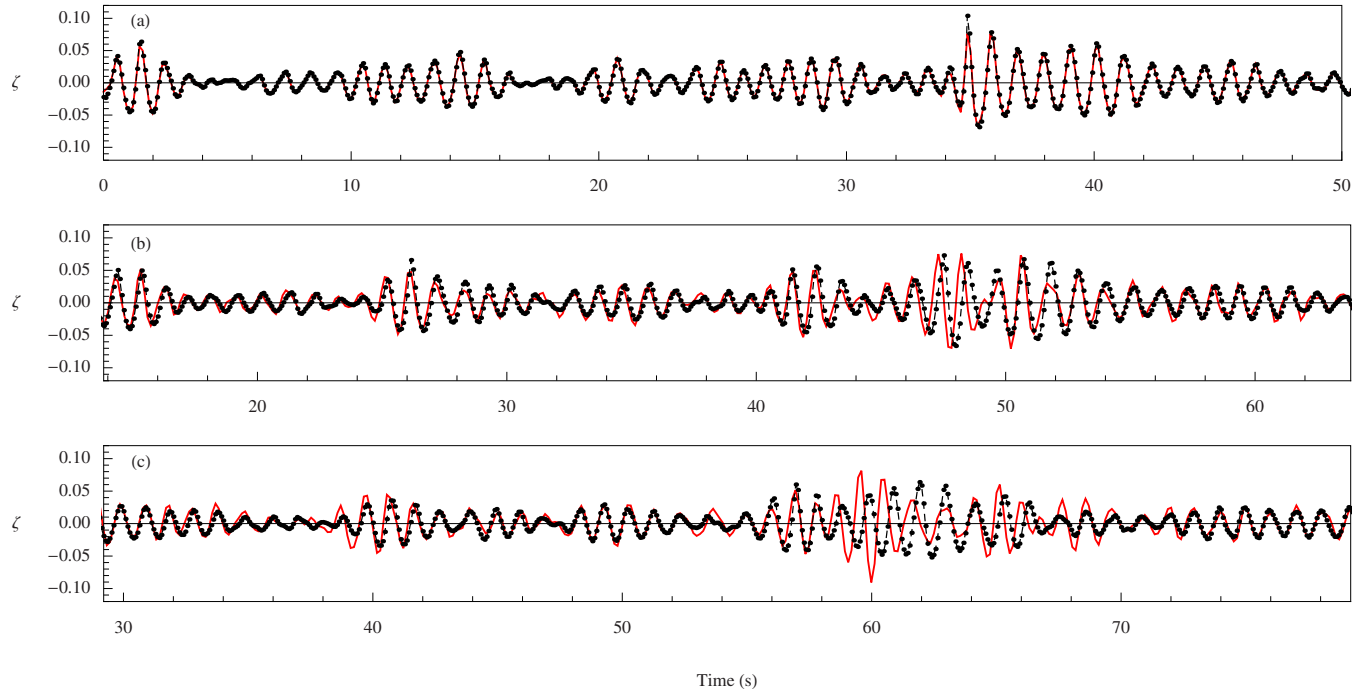

FIG. 9. (Color online) Comparison of the surface elevation for $\gamma=20$ between experimental measurements (dotted line) and numerical solutions of the MNLS equation (solid line) at $x=0$ m, $x=10.8$ m, and $x=22.8$ m (from top to bottom).

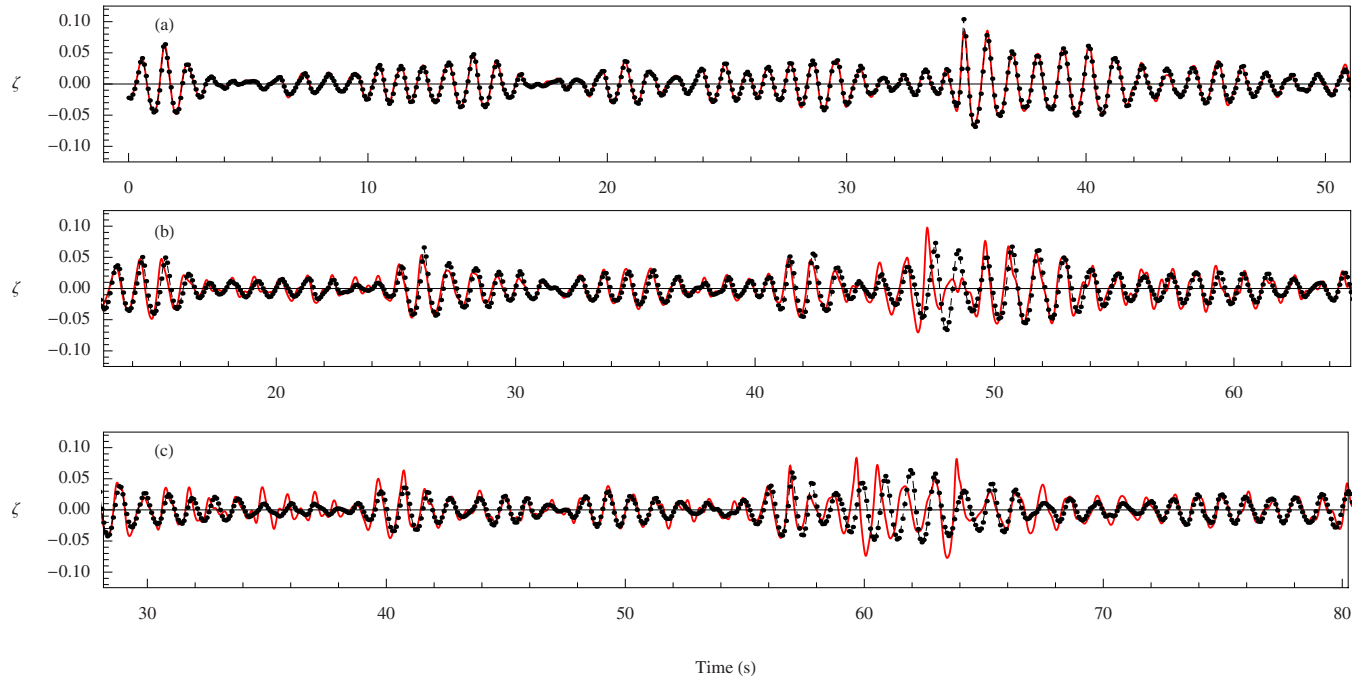

FIG. 10. (Color online) Comparison of the surface elevation for $\gamma=20$ between experimental measurements (dots) and the third-order PS model (solid line) at $x=0$ m, $x=10.8$ m, and $x=22.8$ m (from top to bottom).

tude and phase of surface elevations, with laboratory experiments yet. Initializing the model with a finite number of wave probe measurements is a nontrivial task for short-crested waves and, therefore, an ingenious arrangement of wave probes has to be designed.

Once wave breaking occurs, the PS model fails to describe postbreaking wave fields unless energy dissipation due to wave breaking is parametrized correctly into the model. A preliminary attempt using eddy viscosity terms has been made by Tian *et al.*[17] and the result is found promising. When the eddy viscosity is carefully chosen from laboratory measurements, it has been shown that the measured surface elevation matches well with the numerical solution not only in amplitude but also in phase. An improved eddy viscosity model combined with a reliable breaking criterion is under development and will be incorporated into the PS model. In addition, wind forcing effects need to be modeled properly before the PS model is served as an effective theoretical tool to study the dynamics of nonlinear ocean waves. A combined experimental and theoretical study to parametrize wind effects on steep surface waves is in progress and the PS model with new parametrizations for energy dissipation due to wave breaking and wind forcing will be further validated with laboratory experiments.

ACKNOWLEDGMENTS

This work was supported by the U.S. Office of Naval Research through Grant No. N00014-05-1-0537. The authors gratefully acknowledge partial support from the WCU (World Class University) program through the National Research Foundation of Korea funded by the Ministry of Education, Science and Technology (Grant No. R31-2008-000-10045-0). The authors also thank Okey Nwogu at the University of Michigan and Lawrence Mak at the Institute for Ocean Technology in Canada for their help to set up laboratory experiments, and anonymous reviewers for their careful reading and constructive comments.

APPENDIX A: EXPANSION

Following West *et al.*[1] with a slight modification to include the effect of finite depth, W_n can be found by expanding the vertical velocity $W(\boldsymbol{x},t)\equiv(\partial\phi/\partial z)(\boldsymbol{x},z=\zeta,t)$, in a Taylor series, as

$$W=\sum_{n=1}^{\infty} W_n, \quad W_n=\sum_{j=0}^{n-1} \mathcal{C}_j[\Phi_{n-j}] \quad \text{for } n\geq 1, \tag{A1}$$

where Φ_n is defined by

$$\Phi_1=\Phi, \quad \Phi_n=-\sum_{j=1}^{n-1} \mathcal{A}_j[\Phi_{n-j}] \quad \text{for } n\geq 2. \tag{A2}$$

In Eqs. (A1) and (A2), when all physical variables are written in Fourier series,

$$f(\boldsymbol{x},t)=\sum a(t)e^{i\boldsymbol{k}\cdot\boldsymbol{x}}, \tag{A3}$$

A_n and C_n can be found as

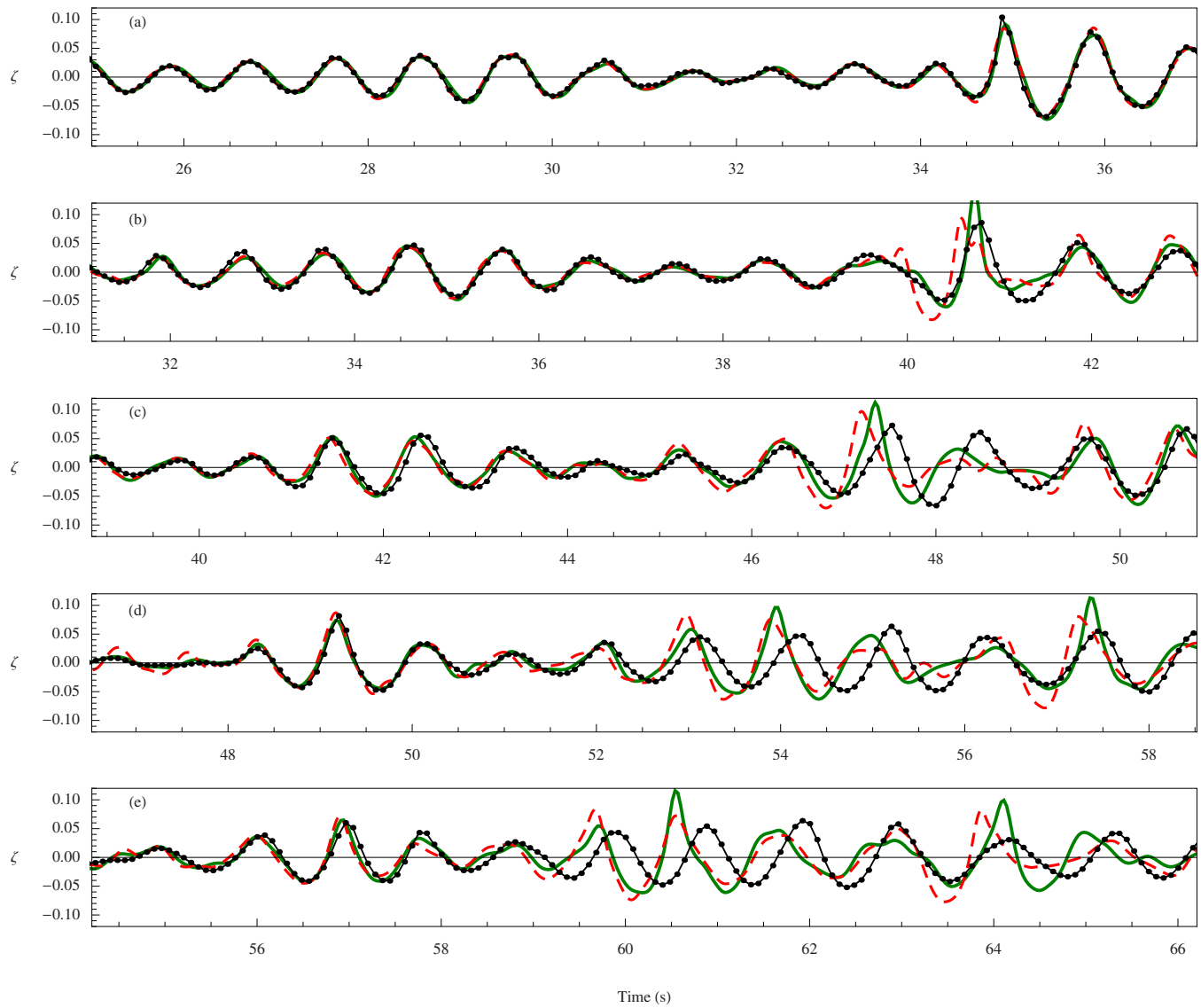

FIG. 11. (Color online) Comparison of the surface elevation for $\gamma=20$ between experimental measurements (dotted line) with the third (dashed line) and fifth-order (thick solid line) PS model at $x=0$, 4.8, 10.8, 16.8, and 22.8 m (from top to bottom).

$$\mathcal{A}_{2m}=\frac{\zeta^{2m}}{(2m)!}k^{2m},\quad \mathcal{A}_{2m+1}=\frac{\zeta^{2m+1}}{(2m+1)!}k^{2m+1}\tanh(kh), \tag{A4}$$

$$\mathcal{C}_{2m}=\frac{\zeta^{2m}}{(2m)!}k^{2m+1}\tanh(kh),\quad \mathcal{C}_{2m+1}=\frac{\zeta^{2m+1}}{(2m+1)!}k^{2m+2}, \tag{A5}$$

where $k=|\boldsymbol{k}|$. The first few terms of W_n and Φ_n given by Eqs. (A1) and (A2) can be written explicitly as

$$W_1=k\tanh(kh)\Phi_1,\quad W_2=k\tanh(kh)\Phi_2+\zeta k^2\Phi_1,$$

$$W_3=k\tanh(kh)\Phi_3+\zeta k^2\Phi_2+\frac{1}{2!}\zeta^2k^3\tanh(kh)\Phi_1,\ \ldots, \tag{A6}$$

$$\Phi_1=\Phi,\quad \Phi_2=-\zeta k\tanh(kh)\Phi_1,$$

$$\Phi_3=-\zeta k\tanh(kh)\Phi_2-\frac{1}{2!}\zeta^2k^2\Phi_1,\ \ldots. \tag{A7}$$

Notice that $W_n=O(\Phi_n)=O(\epsilon^n)$ and they are found recursively as functions of ζ and Φ.

From $W_1=-\mathcal{L}[\Phi]$, the operator $\mathcal{L}$ in Eqs. (6) and (7) can be evaluated in Fourier space as $\mathcal{L}[\Phi]=-k\tanh(kh)\Phi$.

[1]B. J. West, K. A. Brueckner, R. S. Janda, D. M. Milder, and R. L. Milton, "A new numerical method for surface hydrodynamics," J. Geophys. Res. **92**, 11803 (1987).
[2]W. J. D. Bateman, C. Swan, and P. H. Taylor, "On the efficient numerical simulation of directionally spread surface water waves," J. Comput. Phys. **174**, 277 (2001).
[3]M. Tanaka, "Verification of Hasselmann's energy transfer among surface gravity waves by direct numerical simulations of primitive equations," J. Fluid Mech. **440**, 199 (2001).
[4]M. Tanaka, "On the role of resonant interactions in the short-term evolu-

tion of deep-water ocean spectra," J. Phys. Oceanogr. **37**, 1022 (2007).
[5]W. Craig and C. Sulem, "Numerical simulation of gravity waves," J. Comput. Phys. **108**, 73 (1993).
[6]D. G. Dommermuth and D. K. P. Yue, "A high-order spectral method for the study of nonlinear gravity waves," J. Fluid Mech. **184**, 267 (1987).
[7]D. Clamond and J. Grue, "A fast method for fully nonlinear water-wave computations," J. Fluid Mech. **447**, 337 (2001).
[8]R. A. Smith, "An operator expansion formalism for nonlinear surface waves over variable depth," J. Fluid Mech. **363**, 333 (1998).
[9]W. Craig, P. Guyenne, D. P. Nicholls, and C. Sulem, "Hamiltonian long-wave expansions for water waves over a rough bottom," Proc. R. Soc. London, Ser. A. **461**, 839 (2005).
[10]P. Guyenne and D. P. Nicholls, "A high-order spectral method for nonlinear water waves over moving bottom topography," SIAM J. Sci. Comput. (USA) **30**, 81 (2008).
[11]Y. Liu, D. G. Dommermuth, and D. K. P. Yue, "A high-order spectral method for nonlinear wave-body interactions," J. Fluid Mech. **245**, 115 (1992).
[12]C. P. Kent and W. Choi, "An explicit formulation for the evolution of nonlinear surface waves interacting with a submerged body," Int. J. Numer. Methods Fluids **55**, 1019 (2007).
[13]W. Choi, C. P. Kent, and C. J. Schillinger, in *Advances in Engineering Mechanics—Reflections and Outlooks in Honor of Theodore Y.-T. Wu*, edited by A. T. Chwang, M. H. Teng, and D. T. Valentine (World Scientific, Singapore, 2005), pp. 94–110.
[14]D. Fructus, D. Calmond, J. Grue, and O. Kristiansen, "An efficient model for three-dimensional surface wave simulations: Part I: Free space problems," J. Comput. Phys. **205**, 665 (2005).
[15]Z. Tian, M. Perlin, and W. Choi, "Evaluation of a deep-water wave breaking criterion," Phys. Fluids **20**, 066604 (2008).
[16]L. Xu and P. Guyenne, "Numerical simulation of three-dimensional nonlinear water waves," J. Comput. Phys. **228**, 8446 (2009).
[17]Z. Tian, M. Perlin, and W. Choi, "Energy dissipation in two-dimensional unsteady plunging breakers and an eddy viscosity model," J. Fluid Mech. **655**, 217 (2010).
[18]V. E. Zakharov, "Stability of periodic waves of finite amplitude on the surface of a deep fluid," J. Appl. Mech. Tech. Phys. **9**, 190 (1972).
[19]V. P. Krasitskii, "Canonical transformations in a theory of weakly nonlinear waves with a nondecay dispersion law," Sov. Phys. JETP **71**, 921 (1990).
[20]V. P. Krasitskii, "On reduced equations in the Hamiltonian theory of weakly nonlinear surface waves," J. Fluid Mech. **272**, 1 (1994).
[21]M. Stiassnie and L. Shemer, "On modifications of the Zakharov equation for surface gravity waves," J. Fluid Mech. **143**, 47 (1984).
[22]L. Shemer, H. Jiao, E. Kit, and Y. Agnon, "Evolution of a nonlinear wave field along a tank: experiments and numerical simulations based on the Zakharov equation," J. Fluid Mech. **427**, 107 (2001).
[23]N. Yokoyama, "Statistics of gravity waves obtained by direct numerical simulation," J. Fluid Mech. **501**, 169 (1999).
[24]L. Shemer, E. Kit, H.-Y. Jiao, and O. Eitan, "Experiments on nonlinear wave groups in intermediate water depth," J. Waterway, Port, Coastal, Ocean Eng. **124**, 320 (1998).
[25]K. B. Dysthe, "Note on a modification of the nonlinear Schrödinger equation for application to deep water waves," Proc. R. Soc. London, Ser. A **369**, 105 (1979).
[26]K. Trulsen and K. B. Dysthe, "A modified nonlinear Schrödinger equation for broader bandwidth gravity waves on deep water," Wave Motion **24**, 281 (1996).
[27]E. Lo and C. C. Mei, "A numerical study of water-wave modulation based on a higher-order nonlinear Schrödinger equation," J. Fluid Mech. **150**, 395 (1985).
[28]L. Shemer, E. Kit, and H. Jiao, "An experimental and numerical study of the spatial evolution of unidirectional nonlinear water-wave groups," Phys. Fluids **14**, 3380 (2002).
[29]K. Trulsen and C. T. Stansberg, "Spatial evolution of water surface waves: numerical simulation and experiment of bichromatic waves," Proceedings of the 11th International Offshore and Polar Engineering Conference, Stavanger, Norway, 17–22 June 2001 (International Society of Offshore and Polar Engineers, Cupertino, CA, 2001), pp. 71–77.
[30]D. Clamond, M. Francius, J. Grue, and C. Kharif, "Long time interaction of envelope solitons and freak wave formations," Eur. J. Mech. B/Fluids **25**, 536 (2006).
[31]T. B. Johannessen and C. Swan, "Nonlinear transient water waves. Part I. A numerical method of computation with comparisons to 2-D laboratory data," Appl. Ocean. Res. **19**, 293 (1997).
[32]T. B. Johannessen and C. Swan, "A laboratory study of the focusing of transient and directionally spread surface water waves," Proc. R. Soc. London, Ser. A **457**, 971 (2001).
[33]T. B. Johannessen and C. Swan, "On the nonlinear dynamics of wave groups produced by the focusing of surface-water waves," Proc. R. Soc. London, Ser. A **459**, 1021 (2003).
[34]L. Shemer, K. Goulitski, and E. Kit, "Evolution of wide-spectrum unidirectional wave groups in a tank: An experimental and numerical study," Eur. J. Mech. B/Fluids **26**, 193 (2007).
[35]C. A. Spell, J. Zhang, and R. E. Randall, "Hybrid wave model for unidirectional irregular waves-Part II. Comparison with laboratory measurements," Appl. Ocean. Res. **18**, 93 (1996).
[36]J. Zhang, J. Yang, J. Wen, I. Prislin, and R. E. Randall, "Deterministic wave model for short-crested ocean waves: Part I. Theory and numerical scheme," Appl. Ocean. Res. **21**, 167 (1999).
[37]F. Bonnefoy, D. Le Touzé, and P. Ferrant, "A fully-spectral 3D time-domain model for second-order simulation of wavetank experiments. Part B: Validation, calibration versus experiments and sample applications," Appl. Ocean. Res. **28**, 121 (2006).
[38]F. Bonnefoy, D. Le Touzé, and P. Ferrant, "A fully-spectral 3D time-domain model for second-order simulation of wavetank experiments. Part A: Formulation, implementation and numerical properties," Appl. Ocean. Res. **28**, 33 (2006).
[39]J. Grue, D. Clamond, M. Huseby, and A. Jensen, "Kinematics of extreme waves in deep water," Appl. Ocean. Res. **25**, 355 (2003).
[40]K. B. Dysthe, K. Trulsen, H. E. Krogstad, and H. Socquet-Juglard, "Evolution of a narrow-band spectrum of random surface gravity waves," J. Fluid Mech. **478**, 1 (2003).
[41]H. Socquet-Juglard, K. B. Dysthe, K. Trulsen, H. E. Krogstad, and J. Liu, "Probability distributions of surface gravity waves during spectral changes," J. Fluid Mech. **542**, 195 (2005).
[42]M. Onorato, A. R. Osborne, M. Serio, and L. Cavaleri, "Modulational instability and non-Gaussian statistics in experimental random water-wave trains," Phys. Fluids **17**, 078101 (2005).
[43]M. Onorato, A. R. Osborne, M. Serio, L. Cavaleri, C. Brandini, and C. T. Stansberg, "Extreme waves, modulational instability and second order theory: Wave flume experiments on irregular waves," Eur. J. Mech. B/Fluids **25**, 586 (2006).
[44]W. Choi, "Nonlinear evolution equations for two-dimensional waves in a fluid of finite depth," J. Fluid Mech. **295**, 381 (1995).
[45]E. Kit and L. Shemer, "Spatial versions of the Zakharov and Dysthe evolution equations for deep water gravity waves," J. Fluid Mech. **450**, 201 (2002).
[46]T. B. Benjamin and J. E. Feir, "The desintegration of wavetrains on deep water," J. Fluid Mech. **27**, 417 (1967).
[47]I. E. Alber, "The effects of randomness on the stability of two-dimensional surface wavetrains," Proc. R. Soc. London, Ser. A **363**, 525 (1978).
[48]D. A. Crawford, B. M. Lake, P. G. Saffman, and H. C. Yuen, "Effects of nonlinearity and spectral bandwidth on the dispersion relation and component phase speeds of surface gravity waves," J. Fluid Mech. **112**, 1 (1981).
[49]P. A. E. M. Janssen, "Nonlinear four-wave interactions and freak waves," J. Phys. Oceanogr. **33**, 863 (2003).